Eur. Phys. J. D (2019) XXXX: XXXX
https://doi.org/10.1140/epjd/e2019-100106-2

THE EUROPEAN PHYSICAL JOURNAL D

Regular Article

Energy loss of H^+ and H_2^+ beams in carbon nanotubes: a joint experimental and simulation study

Jorge E. Valdés[1,2,5,7], Carlos Celedón[1,2,5,7], Mario Mery[1,2], Juan D. Uribe[1], Rodrigo Segura[3], Néstor R. Arista[4], Isabel Abril[5], and Rafael Garcia-Molina[6,a]

[1] Departamento de Física – Laboratorio de Colisiones Atómicas, Universidad Técnica Federico Santa María, Valparaíso 2390123, Chile
[2] Center for the Development of Nanoscience and Nanotechnology, Centro Basal CEDENNA FB0807, Chile
[3] Instituto de Química y Bioquímica, Facultad de Ciencias, Universidad de Valparaíso, Valparaíso, Chile
[4] Centro Atómico Bariloche, División Colisiones Atómicas, 8400 S.C. de Bariloche, Argentina
[5] Departament de Física Aplicada, Universitat d'Alacant, 03080 Alacant, Spain
[6] Departamento de Física – Centro de Investigación en Óptica y Nanofísica, Regional Campus of International Excellence "Campus Mare Nostrum", Universidad de Murcia, 30100 Murcia, Spain
[7] Donostia International Physics Center DIPC, P. Manuel de Lardizábal 4, 20018 San Sebastián, Spain

Received 26 February 2019 / Received in final form 1 July 2019
Published online (Inserted Later)

Abstract. Carbon nanotube properties can be modified by ion irradiation; therefore it is important to know the manner in which ions deposit energy (how much and where) in the nanotubes. In this work, we have studied, experimentally and with a simulation code, the irradiation of multi-walled carbon nanotubes (MWCNT), supported on a holey amorphous carbon (a-C) substrate, with low energy (2−10 keV/u) H^+ and H_2^+ molecular beams, impinging perpendicularly to the MWCNT axis. The energy distribution of protons traversing the nanotubes (either from the H^+ beam or dissociated from the H_2^+ beam) was measured by the transmission technique in the forward direction. Two well-differentiated peaks appear in the experimental energy-loss distribution of the fragments dissociated from the molecular H_2^+ beam, in correspondence to the ones detected with the proton beam. One is the low-energy loss peak (LELP), which has a symmetric width; the other is the high-energy loss peak (HELP), which shows an asymmetric broadening towards larger energy loss than the corresponding proton energy distribution. A semi-classical simulation, accounting for the main interaction processes (both elastic and inelastic), of the proton trajectories through the nanotube and the supporting substrate has been done, in order to elucidate the origin of these structures in the energy spectra. Regarding the H^+ energy spectrum, the LELP corresponds to projectiles that travel in quasi-channelling motion through the most outer walls of the nanotubes and then pass through the substrate holes, whereas the HELP results mostly from projectiles traversing only the a-C substrate, with the asymmetry broadening being due to a minor contribution of those protons that cross the a-C substrate after exiting the nanotube. The broadening of the peaks corresponding to dissociated fragments, with respect to that of the isolated protons, is the result of vicinage effects between the fragments, when travelling in quasi-channelling conditions through the outer layers of the nanotube, and Coulomb explosion just after exiting the target. The excellent agreement between the measured and the simulated energy spectra of the H^+ beam validates our simulation code in order to predict the energy deposited by ion beams in carbon nanotubes.

1 Introduction

When swift molecules or clusters travel through a solid in a correlated motion, the constituent particles can interact in a coherent way among them and with the medium. Therefore, new physical phenomena can result from these interactions. There are experimental evidences that at high and intermediate projectile energies a significant enhancement of the energy loss of the dissociated fragments appears due to their correlated motion [1,2]. At low projectiles energies (<10 keV/u) experimental data are scarce [3], therefore studies on the irradiation with molecular ions of different targets (in composition and structure) are required.

Carbon nanotubes are promising candidates for many applications in nanoelectronics, computing and data storage, sensors, or detectors [4], among others, due to their nanometer scale, quasi one-dimensional structure and their excellent electrical, mechanical, thermal, and optical

[a] e-mail: rgm@um.es

properties [5]. Additionally, physical properties of carbon nanotubes can be modified by defects at the atomic scale induced by electron or heavy ion irradiation [6,7]. An effective tailoring of their properties could be achieved through irradiation, since the insertion of structural defects into the nanotubes sidewalls leads to a change of their physical and chemical properties [6]. Besides, the little attention devoted to experimental irradiation with hydrogen ions of nanotubes has been restricted to high proton energy (in the MeV range), whereas theoretical works have focused mainly on ion axial channelling through nanotubes, also at high energies [7–9].

In this work, we present experimental energy distributions of fragments resulting from the dissociation of $H_2{}^+$ molecular ions impinging perpendicularly to the main axis of multi-walled carbon nanotubes, in the energy range from 2 keV/u to 10 keV/u. Also, for comparison purposes, the corresponding energy distributions of isotachic proton beams have been measured.

In Section 2, the experimental method is described, where samples of multi-walled carbon nanotubes were synthesized and then dispersed on top of a holey thin amorphous carbon (a-C) substrate and irradiated by energetic $H_2{}^+$ molecular ions and H^+ beams. The measured energy distributions were obtained detecting dissociated molecular fragments as well as the isolated protons transmitted in the forward direction (0° detection angle with a cone detection of 0.5°). For both kinds of beams (H^+ and $H_2{}^+$), two clearly well defined peaks (low energy loss peak, LELP, and high energy loss peak, HELP, hereafter) appear in the energy spectrum and no evidence of molecular recombination was found. Our experimental results show differences in the widths of each one of these peaks when comparing the dissociated $H_2{}^+$ fragments with the case of isotachic isolated protons. In Section 3 a discussion about the origin and interpretation of these peaks is presented, based on a detailed simulation code [10,11] that follows in detail the trajectories of the projectiles through the nanotube and also through the a-C substrate, paying special attention to the interaction with the inhomogeneous electronic density of the MWCNT visited by the protons. Finally, the summary and conclusions of this work are presented in Section 4.

2 Experiment

2.1 Target preparation and characterization

Multi-walled carbon nanotubes were synthesized by the decomposition of a hydrocarbon source, acetylene, over palladium supported catalyst [12,13]. To grow carbon nanotube samples, a thermal chemical vapour deposition apparatus (CVD) was used, which is composed by a horizontal tube furnace, a set of gas flow lines and a quartz tube as reaction chamber. In a typical experiment, 0.01 g of a catalyst composed by 1% of palladium supported on gamma alumina was placed in a quartz boat inside the reaction chamber with a mixture of Ar (200 cm^3/min) and H_2 (100 cm^3/min), where the temperature was kept at 800°C during 10 min. After this annealing, 40 cm^3/min of acetylene was introduced in the furnace during 30 min, maintaining constant the furnace temperature and the Ar/H_2 stream. Following the reaction chamber was cooled down to room temperature under 100 cm^3/min of argon flow. By this process, the acetylene is catalytically decomposed to obtain the nanotubes, which must be purified to eliminate the catalyst. For doing this, the raw sample was treated with NaOH (5%) to eliminate the alumina and with HCl (6 M) to dissolve the palladium particles. After both processes, the sample was filtered with a 0.4 μm pore filter paper and washed thoroughly with abundant distilled water and dried in an argon atmosphere. This manufacturing method to obtain the aqueous solution of nanotubes was done at the Laboratorio de Nanomateriales (Universidad de Valparaíso, Chile) [12,13].

The carbon nanotube samples were characterized by high-resolution Transmission Electron Microscopy (FEI Tecnai G2 F20 S-Twin) and Raman spectroscopy (Deltanu Advantage 532 nm). For TEM measurements, the nanotubes were dispersed on an 18 nm-thick holey amorphous carbon (a-C) film supported by a TEM copper grid. Figure 1 depicts TEM micrographs corresponding to (a) the resulting tangled nanotubes, and (b) a high-resolution image showing the detail of the graphitic walls and the empty channel of a nanotube.

The size of the MWCNTs was estimated by transmission electron microscopy, according to the frequency histogram of the inner and outer diameters of the nanotubes shown in Figure 2a. The statistical analysis reveals that the most probable outer diameter value is around 27 nm, whereas the average inner diameter is close to 5 nm. On the other hand, a complementary identification of the nanotubes was made by Raman spectroscopy. In Figure 2b we depict the Raman spectrum, which exhibits the characteristic peaks corresponding to these kinds of nanotubes, namely, the G-band generated by the E_{2g} vibrational mode and the D-band associated to an active A_{1g} breathing mode of the six-member ring, both linked to vibrational modes of sp^2 bonded carbon atoms [14]. For our carbon nanotubes sample these vibrational modes appear close to 1593 cm^{-1} for the G-band, and 1355 cm^{-1} for the D-band.

2.2 Irradiation setup

Irradiation of the MWCNTs was done using H^+ and $H_2{}^+$ molecular beams generated in a hot discharge ion source, which are focused by an electrostatic lens system and mass selected by a Wien velocity filter. The initial projectile energies, in the range 2−10 keV/u, where calibrated using a 160° spherical electrostatic analyser (ESA) with a resolution better than 1.5%. The irradiation experiments were done in transmission geometry, in a collision chamber with a base pressure of around 10^{-9} Torr, and 10^{-7} Torr during all the measurement procedure. The incident $H_2{}^+$ molecular ions dissociate during the collision with the target, so only molecular fragments are transmitted, and no molecular recombination is observed [3,15]. After the successive collision processes with the MWCNTs and the a-C substrate, the projectiles exit the target and the energy of the

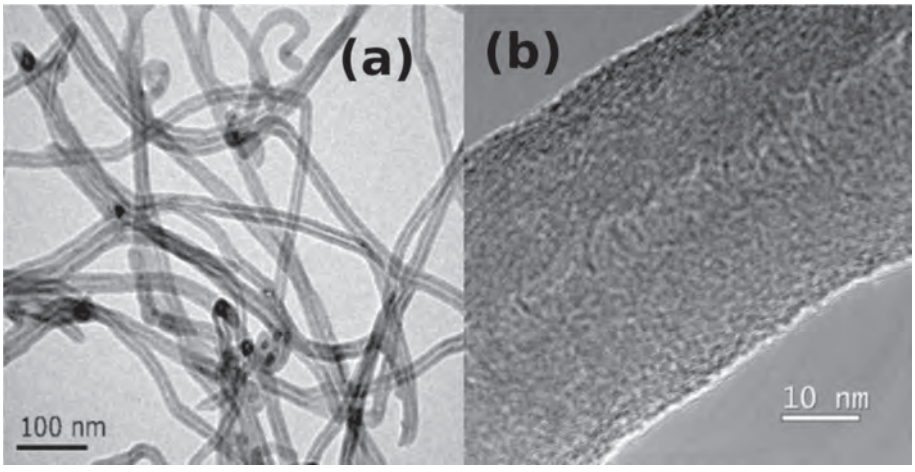

Fig. 1. TEM images of (a) the carbon nanotube mesh, and (b) a portion of a multi-walled carbon nanotube.

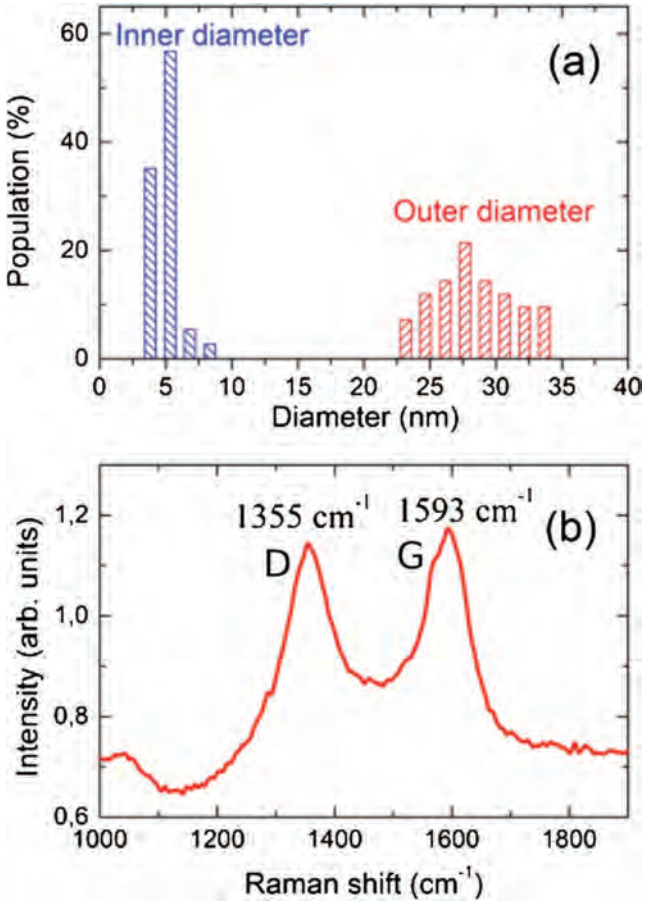

Fig. 2. (a) Frequency histogram of the outer and inner diameters of MWCNTs, as obtained by TEM. (b) Raman spectrum of purified carbon nanotubes used in this experiment, obtained with a 532 nm laser.

outcoming protons, emerging from the dissociation of H_2^+ molecular ions or from the transmitted H^+ beam, is measured in the forward direction (the ESA angular acceptance was 0.5°) and then recorded by a detection system, which uses microchannel plates (MCP) plus counting electronic devices. Energy measurements were done with an error less than 3%. It is pointed out that the overlapping of carbon nanotubes does not introduce detectable signals in the recorded energy spectrum. This is so because the proton (or dissociated fragments) spectrum resulting from stacked MWCNTs have an extremely weak intensity (due to the increased angular deflection) and the energy loss is bigger compared with the one due to a single nanotube, being practically undetectable with our present experimental setup.

2.3 Results

We show in Figure 3 the experimental energy distributions, detected in the forward direction ($0° \pm 0.5°$), of the emerging proton fragments resulting from the dissociation of the H_2^+ molecular ions (blue squares) after interacting with MWCNTs on top of an 18 nm-thick holey a-C film. The initial energy of the beam was (a) $E_0 = 4$ keV/u and (b) $E_0 = 5$ keV/u. The energy spectrum arising from the incidence of isolated protons with the same initial energy per unit mass (i.e., isotachic, with the same velocity) is also depicted (red empty circles). In both cases (dissociated fragments and isolated protons) and for all the energies analysed in this work, we find a similar energy spectrum, with two well-defined peaks, which will be referred to as experimental low energy-loss peak (exp-LELP) and high energy-loss peak (exp-HELP) in what follows [10].

2.4 Data analysis

A detailed comparison between the energy distributions corresponding to fragments and isolated protons presents some interesting features. The exp-LELP in Figures 3a and 3b indicate that the most probable energy loss is similar for fragments and protons, which means that, on average, dissociated fragments lose energy in the same way than isolated protons. This suggests that the interaction

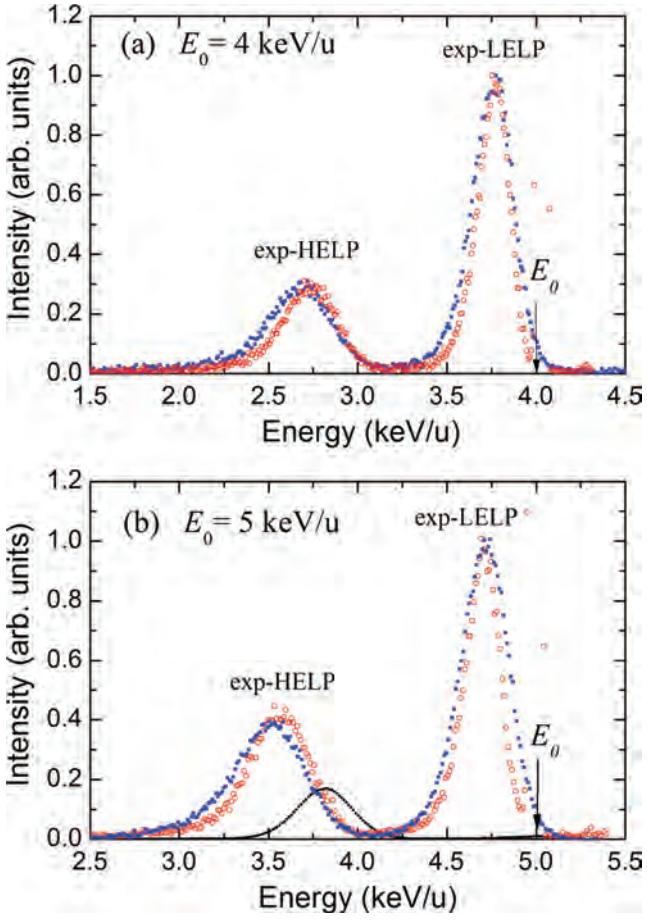

Fig. 3. Experimental energy distribution detected in the forward direction for (a) $E_0 = 4\,\text{keV/u}$ and (b) $E_0 = 5\,\text{keV/u}$ proton fragments dissociated from a $H_2{}^+$ beam (blue squares) and from a H^+ beam (red empty circles) impinging perpendicularly on MWCNTs supported on an 18 nm-thick holey a-C substrate. The small black dots in (b) correspond to the experimental energy distribution for a 5 keV H^+ beam when only traversing the 18 nm-thick a-C substrate. The exp-LELP and exp-HELP labels refer to the low- and high-energy loss peak, respectively.

between the dissociated fragments is weak and does not produce any meaningful change in their energy loss. However, the width of the energy distribution is clearly larger for the fragments compared to the corresponding one for isolated protons. When considering the exp-HELP, the most probable energy is also similar for fragments and isolated protons, within the uncertainties and experimental error. We also notice a slight difference on the right side of the energy-loss distribution, whereas there is a major difference at the high energy-loss flank, where fragments clearly loss more energy than protons. For comparison purposes, we have also depicted in Figure 3b the experimental energy distribution of a proton beam, with the same initial energy per unit mass (i.e., $E_0 = 5\,\text{keV/u}$), incident on a holey a-C foil with a thickness of 18 nm (small black dots). In this case, the most probable proton energy-loss for carbon (i.e., without MWCNTs intercepting the proton beam) lies between the exp-HELP and the

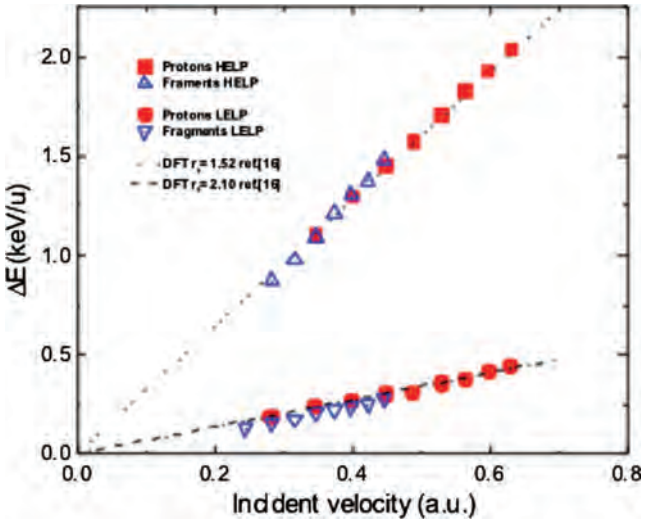

Fig. 4. Most probable energy-loss of the low- (high-) energy loss peak $\Delta E_{\text{exp-LELP}}$ ($\Delta E_{\text{exp-HELP}}$) corresponding to molecular fragments dissociated from $H_2{}^+$, indicated by blue empty down- (up-) triangles, and isolated protons, indicated by red circles (squares), as a function of the incident projectile velocity. The lines represent DFT theoretical results [16] for an electron gas with $r_s = 1.52$ and 2.10 for the high and the low energy-loss peak, respectively.

exp-LELP that appear when the interaction takes place with MWCNTs.

To quantify our findings, Figure 4 shows the most probable energy loss, $\Delta E = E_0 - E_p$, for the low- and the high-energy loss peaks, obtained from the experimental energy distributions of both dissociated fragments and isolated protons, as a function of the incident projectile velocity; E_p is the most probable energy loss in each peak. For comparison purposes, we also show in Figure 4 the theoretical results derived from the density functional theory (DFT) [16], obtained with an electron density parameter $r_s = 1.52$ for the high energy-loss peak and $r_s = 2.10$ for the low energy-loss peak. These values of r_s were used because they correspond to the stopping power that multiplied by the expected value for the average thicknesses traversed by protons (approximately 53 Å for the LELP and 205 Å for the HELP) provide the measured energy losses.

Within the experimental errors, there are not meaningful differences in the most probable energy loss of protons with respect to dissociated fragments, which shows unmistakably the absence of vicinage effects in this quantity. This situation could have been expected due to the nanotube random crystalline structure (as seen by the incident projectiles), which minimizes the mutual interaction between fragments during the passage through the nanotube. A different situation was observed for fragments when passing through targets in channelling conditions, for instance, in single crystal gold, where a significant difference in the energy loss was detected [3].

The fluctuation in the energy loss is quantified through the energy loss straggling variance $\Omega 2 = \langle(\Delta E - \langle \Delta E \rangle)^2\rangle$, where Ω, in eV, is the standard deviation of the energy

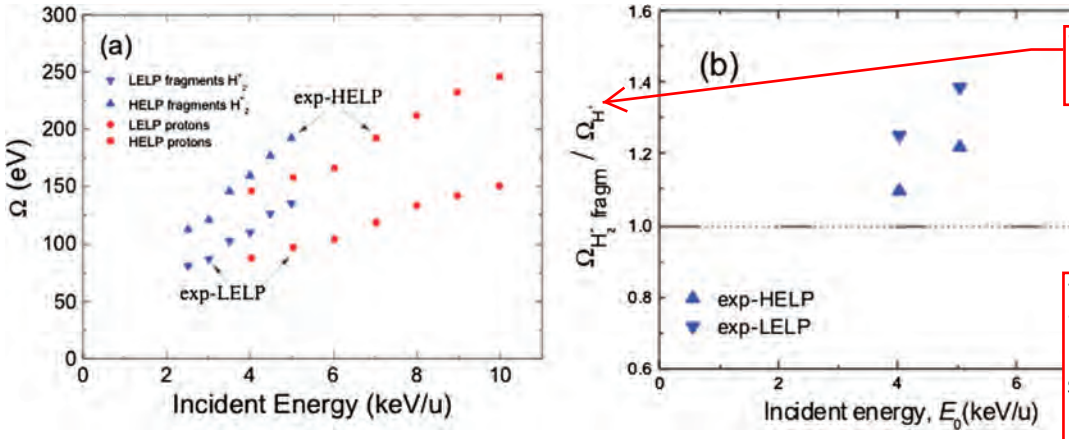

Fig. 5. (a) Straggling, in eV, of the exp-LELP and exp-HELP, obtained from the energy distribution of diss or isolated protons incident on MWCNTs lying on top of an 18 nm-thick holey a-C foil, as a function of the i energy per nucleon. (b) Ratio between the corresponding Ω for the exp-HELP and exp-LELP of transmitt isolated protons incident with $E_0 = 4$ and 5 keV/u.

distribution, which is named energy loss straggling or simply straggling. The value of Ω, obtained from the exp-LELP and the exp-HELP is shown in Figure 5a as a function of the incident energy of the projectile. In Figure 5b we show the ratio between the Ω of each peak for molecular fragments and isolated protons; the respective values for 4 and 5 keV/u are 1.09, 1.21 (for the HELP) and 1.25, 1.39 (for the LELP).

On the other hand, there is an appreciable widening of the fragment's spectrum with respect to protons. These differences are evident in Figure 5a, which shows the straggling, Ω, of the low- and high-energy loss peaks for protons and dissociated fragments from $H_2{}^+$. The corresponding ratio for transmitted fragments and isolated protons at 4 and 5 keV/u incident energies appear in Figure 5b. The differences observed in the case of the low energy-loss peaks can be ascribed to the so-called "vicinage effect", and they are in qualitative good agreement with previous theoretical predictions [17] and experimental findings for dissociated molecular fragments moving under channelling conditions in the low-energy range [18–20]. The differences in the width of the energy loss corresponding to the high energy-loss peaks are not attributable to "vicinage effect", since this result is mainly due to the joint contribution of the MWCNT and substrate to the increase of the thickness traversed by the projectiles, which results in broader energy distributions.

The measured wider energy distribution for the fragments as compared to the isolated protons is in good agreement with the behavior reported by Gridneva et al. [21], who studied the interaction of $H_2{}^+$ molecular ions with carbon foils. However, these authors did not detect vicinage effects in the energy loss because their target does not offer the possibility of channeling as compared with previous experiments [3].

A more detailed discussion on the larger broadening of the fragments distribution will be provided in what follows, on the basis of the results obtained from a simulation code [10].

3 Simulation

3.1 Origin of the peaks in the energy spectrum

The main feature of the experimental energy distribution of the transmitted protons in the forward direction, when $H_2{}^+$ molecular ions or isolated H^+ impact on MWCNTs perpendicular to their axes, is the presence of two well defined peaks, which appear for the dissociated fragments as well as for the isolated protons. To elucidate the origin of these peaks we use a semiclassical simulation performed for the case of a H^+ beam that accounts for in a detailed manner the interaction forces felt by each projectile along its trajectory through the target (MWCNT, and a-C substrate when applicable). Although a description of the simulation procedure has been published elsewhere [10], a summary of its major features is presented in what follows, in order to facilitate the discussion about the origin of the peaks in the energy spectrum.

The size and configuration of the MWCNT used in the simulation are analogous to the experimental ones, corresponding to average inner and outer diameters of 5 nm and 27 nm, respectively, as shown in Figure 2a. The position of the carbon atoms in each wall of the nanotube is generated by rolling a graphene sheet, where the chirality and the distance between walls of the nanotube have been properly considered [22]. The position and velocity of each projectile through the MWCNT (and the a-C substrate, when appropriate) are obtained as a function of time by solving numerically its equation of motion by means of Verlet's algorithm [23]. The elastic interaction between the projectile and the carbon nuclei, which only modifies the direction of the former but not its speed, is modelled by a Lenz-Jensen type potential [24]. The recoil of the carbon atoms is ignored because they are bound to the network and also due to the large mass difference with the projectile.

The electronic stopping force that undergoes the projectile due to inelastic interactions with the target electrons is evaluated from a non-linear density functional theory

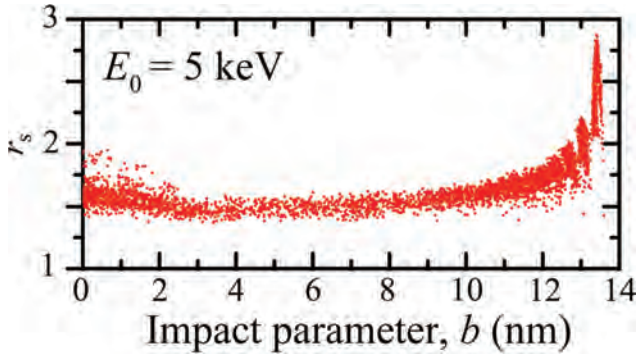

Fig. 6. Wigner-Seitz radius r_s corresponding to the electronic densities visited by 5 keV protons incident on a MWCNT ($D_{\text{in}} = 5$ nm, $D_{\text{out}} = 27$ nm) with different impact parameters b.

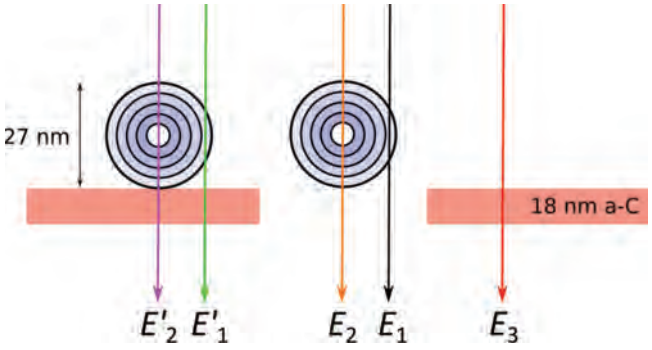

Fig. 7. Main trajectories of the projectiles that pass through the MWCNT and holey a-C substrate. E_1 and E_2 correspond to projectiles that pass through the outer and inner walls, respectively, of nanotubes located on the holes of the amorphous carbon substrate. E'_1 and E'_2 relate to projectiles that, besides traversing the same regions than previously, also pass through the a-C substrate. Projectiles that only cross through the a-C substrate are represented by E_3.

(DFT) for a free electron gas [16], where the average stopping force is proportional to the projectile speed. Stochastic fluctuations in the stopping force are included through the energy-loss straggling, Ω^2, which is proportional to the square of the projectile speed [25]. The proportionality constants of the stopping power and the energy loss straggling depend on the local electronic density visited by the projectile in its travel through the nanotube and/or the a-C substrate. The strong localization of the electronic density around the carbon atoms of the nanotube implies that the projectile explores regions with very different electronic densities, which were implemented by the ab initio TB-LMTO method [26,27].

In each one of the 10^6 simulated histories, protons with initial energy E_0 are sent with a random impact parameter b perpendicularly to the nanotube, whose inner and outer diameters are D_{in} and D_{out} respectively. Due to the chirality of the MWCNT, a random rotation around its main axis is performed in order to emulate the experimental random orientation of the nanotubes. We show in Figure 6 the electronic densities (characterized by their Wigner-Seitz radius r_s) explored by the projectiles when simulating the incidence of a 5 keV proton beam with different impact parameters on a MWCNT having inner and outer diameters $D_{\text{in}} = 5$ nm and $D_{\text{out}} = 27$ nm, respectively. It can be seen that for impact parameters b less than ∼12 nm (i.e., projectiles traversing the MWCNT through its inner walls), most of the electronic densities are characterized by a value of $r_s \approx 1.5$. When the projectiles travel through the outermost walls ($b > 12$ nm) a sharp peak-and-valleys structure appear in the values of r_s visited by the projectile, which corresponds to projectiles moving in quasi-channelling conditions; in this case, the projectiles interact with low electronic density regions as evidenced by the greater value of the Wigner-Seitz radius, $r_s > 2$.

The electronic densities visited by the projectiles not only determine their energy loss, but also their charge state, due to the processes of electron capture and loss. Due to the scarcity of experimental H^+ and H_0 fractions at the low energies considered in this work, we use the value for $r_s \approx 1.5$ (corresponding to a graphite or an amorphous carbon target [28]) provided by the CasP code [29]. In this the case, only 5% of the projectiles traversing the inner walls of the MWCNT emerge as protons, whereas most of them (95%) are neutral hydrogen and cannot be detected by the electrostatic analyser. For obtaining the charge fractions corresponding to the lower densities ($r_s \approx 2$) explored by the projectiles traveling through the outermost walls, we use the data provided for aluminium [30], which has a similar r_s value [28]. In this case, there is a higher (>10%) percentage of protons exiting the nanotube. Then, in order to reproduce the experimental results, in what follows we will consider that protons reaching the detector have traversed the outer walls or the inner walls of the MWCNT in a proportion of ∼2:1.

Besides protons passing through the nanotube, the simulation also includes the interaction of the protons with the a-C substrate, either directly or after traversing the nanotube. In this case, the fraction of H^+ is the same than for the inner walls of the MWCNT, as in both cases $r_s \approx 1.5$ because these walls resemble a graphite target [28]. Leaving aside the protons that pass through the substrate holes without losing energy, Figure 7 depicts schematically the different types of projectile trajectories that eventually will reach the detector in the forward direction: projectiles that move through the outer or inner walls of the nanotubes (denoted by E_1 and E_2, respectively) situated on the holes of the a-C foil, those projectiles that further cross the a-C foil (represented by E'_1 and E'_2) and, finally, the projectiles that are crossing directly through the amorphous carbon substrate (denoted by E_3).

Figure 8a depicts the main contributions to the energy spectrum of projectiles exiting in the forward direction ($0° \pm 0.5°$), resulting from a 5 keV proton beam that impinges on a MWCNT ($D_{\text{in}} = 5$ nm, $D_{\text{out}} = 27$ nm) on top of the holey 18 nm-thick a-C substrate. The different spectra are shown in the same scale (normalized to their maximum) in order to visualize their main features (position and shape). The different histograms represent the energetic distribution of projectiles passing through: the external walls ($b > 12$ nm) of the MWCNT on top of the holes (black line), the inner walls ($b < 12$ nm) of the

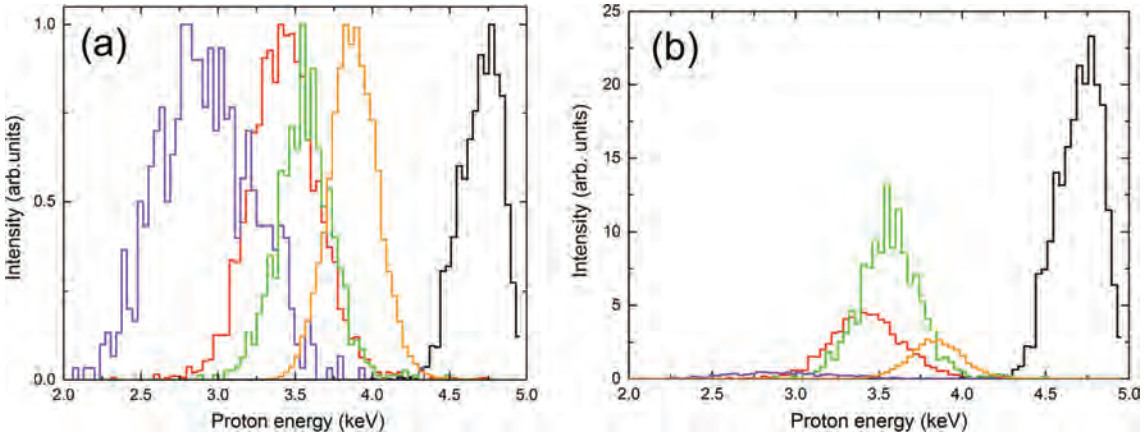

Fig. 8. (a) Simulated energy distributions (normalized to their maxim value) contributing to the spectrum of projectiles in the forward direction ($0^\circ \pm 0.5^\circ$) for a 5 keV proton beam impinging perpendicularly on a MWCNT ($D_{\text{in}} = 5$ nm, $D_{\text{out}} = 27$ nm) on top of an 18 nm-thick holey a-C substrate: (black line ___) projectiles passing through the external walls ($b > 12$ nm) of the MWCNT on top of the holes, (orange line ___) projectiles passing through the inner walls ($b < 12$ nm) of the MWCNT on top of the holes, (green line ___) projectiles passing through the a-C substrate, (red line ___) projectiles passing through the external walls ($b > 12$ nm) of the MWCNT and the a-C substrate, and (purple line ___) projectiles passing through the inner walls ($b < 12$ nm) of the MWCNT and the a-C substrate. (b) The same distributions weighted with the fraction of protons reaching the detector in each case, as well as the proportion of holes (30%) and a-C substrate (70%).

MWCNT on top of the holes (orange line), the a-C substrate (green line), the external walls ($b > 12$ nm) of the MWCNT on top of the a-C substrate (red line), and the inner walls ($b < 12$ nm) of the MWCNT on top of the a-C substrate (purple line).

In order to obtain a reliable simulation that could reproduce the experimental data, the distributions shown in Figure 8a must be weighted with the percentages of a-C substrate (∼70%) and holes (∼30%), as well as by the fraction of protons reaching the detector in each case, according to the r_s values visited, as discussed previously. The contribution to the final energy spectrum of each one of the previous distributions appears depicted in Figure 8b.

In Figure 9 we compare the experimental and the simulated energy distributions of protons detected in the forward direction, resulting from the interaction of a 5 keV proton beam with MWCNTs on top of an 18 nm-thick holey a-C substrate, whose characteristics have been described previously. There is a good agreement between the experimental energy loss distribution, taken from Figure 3b, and the simulation, taken from Figure 8b. The position and shape of the two distinct peaks as well as the valley between them are clearly reproduced in the simulation. The widths of the peaks are not so well reproduced, probably due to minor differences between the idealized system studied in the simulation, as compared to the experimental situation (a broad range of MWCNT sizes and orientations dispersed on the holey amorphous carbon substrate).

Therefore, according to the previous discussion, the origin of the LELP can be clearly ascribed to protons that pass through the holes in the a-C substrate after having travelled in quasi-channelling conditions through the outermost walls of the MWCNT, whereas the HELP results mostly from protons that have traversed the a-C substrate, with minor contributions (to the distribution

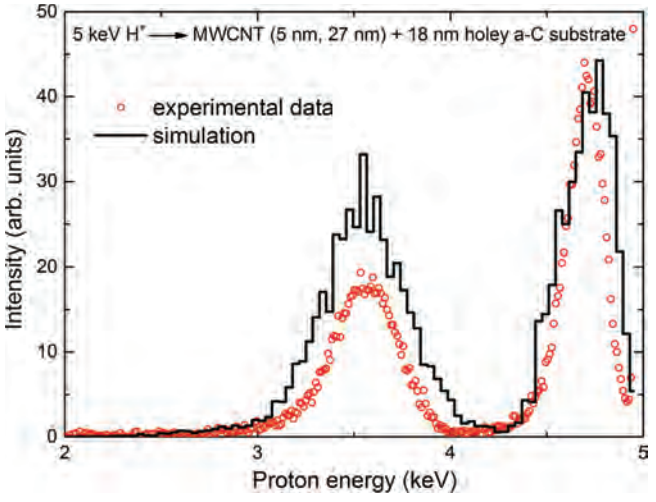

Fig. 9. Simulated (histogram) and experimental (symbols) energy distribution of protons detected in the forward direction ($0^\circ \pm 0.5^\circ$), after a 5 keV proton beam impinges perpendicularly on MWCNTs (with internal and external diameters $D_{\text{in}} = 5$ nm and $D_{\text{out}} = 27$ nm) on top of a holey 18 nm a-C substrate. Both sets of data have been normalized to the maximum of the LELP.

width) from protons that interacted with the MWCNT before passing through the a-C substrate.

3.2 Energy distribution of the dissociated H_2^+ fragments

The differences that appear in the experimental energy loss distribution for H_2^+ fragments in comparison with isolated H^+ (cf. Figs. 3–5) can be attributed to the

vicinage effects arising during the propagation of the dissociated fragments [17,32], which cause the alignment of the trailing fragment with the leading one [33] and the Coulomb repulsion between both fragments, which broadens the energy spectrum of the fragments with respect to the isolated protons, as clearly can be seen in Figure 5 for the exp-LELP. Since the projectiles contributing to this peak travel a short distance through regions of low electron density (in quasi-channelling conditions through the most outer walls of the MWCNTs), there are practically not interference effects between both fragments, and the mean energy is essentially the same for the dissociated fragments and isotachic isolated protons.

Although the width of the high energy-loss peak corresponding to the dissociated fragments is also larger than for the isolated protons (Fig. 5), this cannot be ascribed only to vicinage effects, since the ratio of widths depicted in Figure 5b is closer to unity than for the low energy-loss peak. The distributions of the dissociated fragments and isolated protons emerging in the forward direction after quasi-channelling through the nanotube (i.e., those causing the low energy loss distributions) are further broadened when crossing the a-C foil, due to multiple scattering and wider thickness. Therefore, the exp-HELP distribution mimics the exp-LELP distribution, but is wider due to the extra elastic scattering with the a-C substrate, for both the dissociated fragments and the isolated protons. In this case, the dissociated fragments have a broader energy distribution because they enter the a-C foil with an initial energy distribution that is already wider than the one corresponding to the isolated protons, but no further broadening is produced through the a-C target. The reduced intensity of the HELP with respect to the LELP reflects the fact that many protons are deviated from the forward direction after traversing the a-C foil.

4 Summary and conclusions

In this work we have measured the energy spectra of protons detected in the forward direction resulting from low energy (2−10 keV/u) $H_2{}^+$ and H^+ beams interacting with multiwalled carbon nanotubes lying on top of a holey amorphous carbon substrate. Two distinct peaks appear for protons dissociated from the incident $H_2{}^+$ beam as well as for the isotachic isolated proton beam. The origin of these peaks, as well as their main features (most probable energy and energy width) are interpreted at the light of a simulation that includes the main interaction processes taking place between a beam of protons and a MWCNT ($D_{\rm in} = 5$ nm, $D_{\rm out} = 27$ nm) on top of an 18 nm-thick holey a-C substrate. The low energy-loss peak in the energy distribution results from protons that travel in quasi-channelling conditions through the most external walls of the MWCNT and reach the detector after passing through the holes of the a-C film. On the other hand, the high energy-loss peak is produced mainly by to those protons that travel through the a-C substrate, with a minor contribution (to the asymmetry of the distribution, mainly) of those protons that after being channelled through the outermost walls of the MWCNTs also pass through the a-C substrate; this explain the larger energy loss as well as the broader energy distribution of the high energy-loss peak with respect to the low energy-loss peak.

The fragments dissociated from the $H_2{}^+$ ion that move in quasi-channelling conditions through the nanotube experience sizable vicinage effects, which manifest in the widening of the low energy-loss peak of the fragments with respect to that of the isolated protons. This larger widening is not seen in the high-energy loss peak of the dissociated fragments as compared to the isolated protons, since they are decorrelated due to multiple scattering when moving through the a-C foil that supports the MWCNT.

This work has been financially supported by Fondecyt 1100759, Fondecyt 1121203 and USM-DGIP 11.11.11, Anillo ACT1108, the Spanish Ministerio de Economía y Competitividad and European Regional Development Fund (Projects FIS2014-58849-P and PGC2018-096788-B-I00), and Fundación Séneca (Project No. 19907/GERM/15). J.E.V. acknowledges the hospitality at Department de Física Aplicada (Universitat d'Alacant) and the DIPC-San Sebastián; he also thanks to I. Nagy and V.A. Esaulov for very interesting and useful discussions and P. Vargas for his help with TB-LMTO calculations for electron densities.

Author contribution statement

J.E.V. designed the project and together with C.C., M.M. and J.D.U. performed the experiment and carried out data analysis. R.S. prepared the MWCNT, providing their characterization and samples in a suitable substrate for irradiation. J.E.V., R.G.M., I.A. and N.R.A. modelled and discussed the results of the simulations, providing the explanations when comparing with the experimental data. All authors contributed to manuscript writing and general discussions.

References

1. S.M. Shubeita, P.L. Grande, J.F. Dias, R. Garcia-Molina, C.D. Denton, I. Abril, Phys. Rev. B **83**, 245423 (2011)
2. N.E. Koval, A.G. Borisov, L.F.S. Rosa, E.M. Stori, J.F. Dias, P.L. Grande, D. Sánchez-Portal, R. Díez Muiño, Phys. Rev. A **95**, 062707 (2017)
3. J.E. Valdés, C. Parra, J. Díaz-Valdés, C.D. Denton, C. Agurto, F. Ortega, N.R. Arista, P. Vargas, Phys. Rev. A **68**, 064901 (2003)
4. R.H. Baughman, A.A. Zakhidov, W.A. de Heer, Science **297**, 787 (2002)
5. M.S. Dresselhaus, G. Dresselhaus, P. Avouris, *Carbon Nanotubes, Synthesis, Structure, Properties and Applications* (Springer, Berlin, 2001)
6. A.V. Krasheninnikov, K. Nordlund, J. Appl. Phys. **107**, 071301 (2010)
7. A. Olejniczak, V.A. Skuratov, Nucl. Instrum. Methods Phys. Res. **326**, 33 (2014)
8. Y. Zhang, L. Chen, Z. Xu, Y. Li, M. Shan, L. Liu, Q. Guo, G. Chen, Z. Wang, C. Wang, Int. J. Mat. Prod. Technol. **45**, 1 (2012)

9. Z.L. Mišković, Radiat. Eff. Def. Sol. **162**, 185 (2007)
10. J.E. Valdés, C. Celedón, R. Segura, I. Abril, R. Garcia-Molina, C.D. Denton, N.R. Arista, P. Vargas, Carbon **52**, 137 (2013)
11. C.E. Celedón, A. Cortés, E.A. Sánchez, M.S. Moreno, J.D. Uribe, N.R. Arista, J.E. Valdés, Eur. Phys. J. D **71**, 64 (2017)
12. R.A. Segura, A. Tello, G. Cárdenas, P. Häberle, Phys. Stat. Sol. (a) **204**, 513 (2007)
13. I. Kyriakou, C. Celedón, R. Segura, D. Emfietzoglou, P. Vargas, J.E. Valdés, I. Abril, C.D. Denton, K. Kostarelos, R. Garcia-Molina, Nucl. Instrum. Meth. Phys. Res. B **268**, 1781 (2010)
14. R.A. Segura, S. Hevia, P. Häberle, J. Nanosci. Nanotechnol. **11**, 10036 (2011)
15. R. Garcia-Molina, M.D. Barriga-Carrasco, Phys. Rev. A **68**, 054901 (2003)
16. P.M. Echenique, R.M. Nieminen, R.H. Ritchie, Solid State Commun. **37**, 779 (1981)
17. N.R. Arista, Nucl. Instrum. Meth. Phys. Res. B **164–165**, 108 (2000)
18. J.C. Eckardt, G.H. Lantschner, N.R. Arista, R.A. Baragiola, J. Phys. C **11**, L851 (1978)
19. R. Levi-Setti, K. Lam, T.R. Fox, Nucl. Instrum. Methods Phys. Res. **194**, 281 (1982)
20. E.A. Figueroa, E.D. Cantero, J.C. Eckardt, G.H. Lantschner, M.L. Martiarena, N.R. Arista, Phys. Rev. A **78**, 032901 (2008)
21. E.A. Gridneva, N.N. Koborov, V.A. Kurnaev, N.N. Trifonov, JETP Lett. **1**, 15 (2003)
22. W.W. Ruland, A.K. Schaperb, H. Houa, A. Greinera, Carbon **41**, 423 (2003)
23. M.O. Allen, D.J. Tildesley, *Computer Simulation of Liquids* (Oxford University Press, Oxford, 1989)
24. W. Eckstein, *Computer Simulation of Ion-solid Interactions* (Springer-Verlag, Berlin, 1991)
25. C.E. Celedón, E.D. Cantero, G.H. Lantschner, N.R. Arista, Nucl. Instrum. Methods Phys. Res. B **315**, 21 (2013)
26. O.K. Andersen, O. Jepsen, Phys. Rev. Lett. **53**, 2571 (1984)
27. O.K. Andersen, Z. Pawlowska, O. Jepsen, Phys. Rev. B **34**, 5253 (1986)
28. D. Isaacson, *Compilation of r_s Values, Internal Report, Radiation and Solid State Laboratory* (New York University, New York, 1975)
29. G. Schiwietz, P.L. Grande, Nucl. Instr. Meth. B **175–177**, 125 (2001)
30. J.A. Phillips, Phys. Rev. **97**, 404 (1955)
31. R. Garcia-Molina, I. Abril, C.D. Denton, S. Heredia-Avalos, Nucl. Instrum. Methods Phys. Res. B **249**, 6 (2006)
32. P. Sigmund, *Particle Penetration and Radiation Effects Vol. 2: Penetration of Atomic and Molecular Ions* (Springer, 2014)
33. M.D. Barriga-Carrasco, R. Garcia-Molina, Phys. Rev. A **68**, 062902 (2003)